Geomechanics of hydraulic fracturing microseismicity: Part 1. Shear, hybrid, and tensile events

Seth Busetti, Wenjie Jiao, and Ze'ev Reches

ABSTRACT

We investigate the geomechanical behavior of hydraulic-fracturing-induced microseismicity. Microseismic events are commonly used to discern stimulation patterns and hydraulic fracture evolution; however, techniques beyond fracture mapping are required to explain the mechanisms of microseismicity. In this series we present an approach to combine seismological and geomechanical techniques to investigate how microseismicity relates to propagating hydrofractures as well as existing natural fractures and faults. Part 1 describes the first analysis step, which is to characterize the microseismic events by their source parameters, focal mechanisms, and fault-plane orientations. These parameters are used to determine the mechanical conditions responsible for activation of discrete populations or subpopulations of microseismic events that then can be interpreted in their geological and operational context. First, we compare microseismic fault-plane populations from a Mississippian Barnett Shale, Texas data set that are determined using a traditional double-couple model (shear only) with a tensile source model (hybrid events), which may be more suitable for hydraulic fracturing conditions. Second, we employ a new method to distinguish fault planes from auxiliary planes using iterative stress inversion and critical stress (instability) selection criteria. The result is an enhanced microseismic characterization that includes geomechanical parameters such as slip tendency and local activation stress state during the operation. Using this approach on the Barnett Shale data, two microseismic fault sets are resolved: an inclined northeast–southwest set with dominant shear, and a vertical north–south set

Manuscript received July 15, 2013; provisional acceptance January 16, 2014; revised manuscript received February 03, 2014; final acceptance May 14, 2014.
DOI: 10.1306/05141413123

AUTHORS

SETH BUSETTI ~ *ConocoPhillips, 600 N. Dairy Ashford, Houston, Texas 77079; seth.busetti@conocophillips.com*

Seth Busetti received a B.S. degree in geological engineering from the Colorado School of Mines and an M.S. degree and Ph.D. in structural geology from the University of Oklahoma. Busetti is currently employed by ConocoPhillips and works in a subsurface technology position focusing on applied structural geology and geomechanics problems worldwide. He is involved in projects involving fracture and fault mechanics, fluid flow in fractured reservoirs, and geomechanics in non-conventional reservoirs.

WENJIE JIAO ~ *ConocoPhillips, 600 N. Dairy Ashford, Houston, Texas 77079; wenjie.jiao@conocophillips.com*

Wenjie Jiao received a B.S. degree in structural geology and geophysics from Nanjing University, an M.S. degree in rock mechanics from Institute of Geology, State Seismological Bureau, China, and a Ph.D. in seismology from University of Arizona. He worked mainly in monitoring geophysics for more than 13 years before joining the petroleum industry. Currently, he is a staff geophysicist with ConocoPhillips.

ZE'EV RECHES ~ *University of Oklahoma, ConocoPhillips School of Geology and Geophysics, 100 East Boyd Street Suite 710, Norman, Oklahoma 73019; reches@ou.edu*

Ze'ev Reches received B.S. and M.S. degrees in geology from Hebrew University, Israel, and a Ph.D. in structural geology from Stanford University. Reches serves as professor of structural geology at the University of Oklahoma. His prior work includes positions at Arizona State University, Stanford University, and US Geological Survey at Menlo Park, California, and Hebrew University, Israel. Research interests include earthquake and fault processes and rock mechanics.

ACKNOWLEDGEMENTS

We thank ConocoPhillips Technology and ConocoPhillips Mid-Continent Business Unit for permission to publish the data and our findings. Brad Bankhead and his team developed the Stocker geophysical research program and encouraged this geomechanical effort. We thank Ted Dohmen, Mark Willis, Samik Sil, Joe Zhou, Ray Reid, Pijush Paul, Peter Hennings, Raoul Treverton, Anastasia Mironova, Bruce Hart, and the many other technical contributors to the project. We appreciate the thoughtful feedback on technical framing and analysis from ConocoPhillips' Seismic Analysis group who helped substantiate continuation of the research. Microseismic processing and moment-tensor inversion (MTI) was performed by Magnitude, Baker Hughes. Most of the calculations and advanced plots were done using MATLAB. We also used fracture plotting tools in FracMan (Golder Associates). Lastly, thanks to Alan Morris, David Haddad, Daniel Moos, and an anonymous reviewer for reviewing the manuscript and providing very helpful comments and edits.

The AAPG Editor and special issue editor David A. Ferrill thank the following reviewers for their work on this paper: David E. Haddad, Daniel Moos, Alan P. Morris, and an anonymous reviewer.

with more hybrid behavior. The results are used in part 2 to further investigate the heterogeneity of the stimulations and to compare models for microseismic activation.

INDUCED ROCK FAILURE DURING HYDROFRACTURING

Injection of a hydrofracture into a reservoir or the emplacement of an igneous dike into the crust should perturb the in situ stress field in the surrounding rocks. The stress perturbation can activate a multitude of pre-existing discontinuities as evident by microseismic events recorded during hydrofracturing, or similarly, faults and fractures associated with exposed dike systems. For example, Pollard et al. (1975) mapped three-dimensional (3-D) dike segments and fingers indicating that the actual propagation mechanism during dike emplacement is more complicated than sheet-like tensile-fracture-extension concepts predict. Baer (1991) found similar dike morphologic features, with segments displaying intermittent smooth patches and slickensides, which indicate both tensile and shear mechanisms are active during dike extension. Tensile and shear activation of features off the main plane of a hydrofracture is not limited to a stress perturbation alone. Injected fluids may penetrate into pre-existing discontinuities of the host rocks (Warpinski and Teufel, 1987), and activate them by combined shear, dilation, and brecciation (Delaney and Pollard, 1981). For example, the microseismicity at Inyo crater, California, revealed both double-couple and dilational events associated with the local igneous activity (Sipkin, 1985; Reches and Fink, 1988). Thus, one may expect that microseismicity associated with hydrofracturing will be complex and include a wide range of failure styles.

Our main objective is to investigate the hydrofracturing process by detailed analysis of the associated microseismicity. We assume that the microseismic events belong to a continuum with three classical end members (Figure 1): (1) a joint, which is a fracture dilated by pressurized fluid or tensile failure and the dilational displacement that is normal to the fracture surface (Figure 1E); (2) a fault, which is a shear fracture with slip parallel to its surface (dip slip, strike slip, or oblique), (Figure 1C); and (3) a compaction band with shortening normal to the fracture surface (Figure 1A). The transition cases between these end members include the dilational fault and the compacting fault (Figure 1B, D). Hybrid (or mixed-mode) failure and oblique slip have been well documented at all scales (e.g., Mandl, 1988; Engelder, 1999; Ramsey and Chester, 2004; Ferrill et al., 2012) and also are apparent from microseismic data. Our approach is

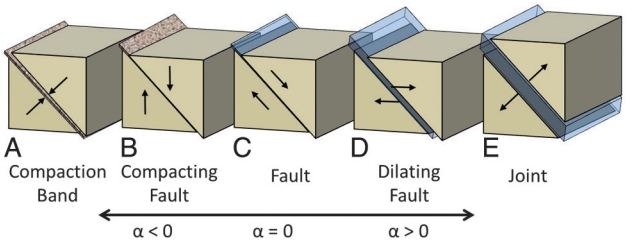

Figure 1. Concept model for shear, hybrid, and tensile microseismic activation. Case shown is for a pure dilatant dip-slip microseismic event. The cartoon depicts increasing angle α, the angle between the slip direction and the fault plane, related to the presence of fluid (blue).

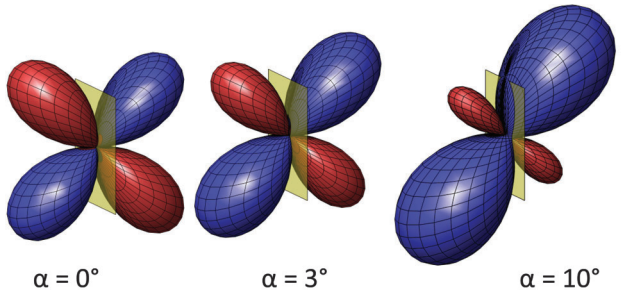

Figure 2. Seismic radiation patterns as a function of inclination angle α. Color indicates polarity, with sign from +1 (red) to −1 (blue). With increasing α, the pattern becomes more asymmetric. One of the two possible focal planes is shown in yellow for reference.

to identify these secondary fractures in the focal mechanisms data of hydrofracturing microseismicity, and to resolve the stress fields active during the hydraulic fracturing.

The study has two parts. Part 1 presents the analytical tools needed to determine the source parameters, focal mechanisms, and fault-plane orientations. These tools are applied in part 2 (Busetti and Reches, 2014, this issue) for detailed geomechanical analysis of a case study of hydrofracturing in the Mississippian Barnett Shale, Texas. In the first part, we consider the complete range of source mechanisms of failure (Figure 1), and deviate from the common microseismic analyses that assume that all focal mechanisms are for double-couple events. We primarily follow the analysis of Vavryčuk (2001, 2011) who coined the term tensile earthquake to account for fault slip that is not parallel to the fault plane, for example, the dilation or compacting fault of Figure 1. The parameter α is related to the seismic radiation patterns (Figure 2) and is used to indicate the inclination of the resolved slip vector off of the plane. Because the term "inclination angle" is commonly used for the dip of a fault, we instead use the term "deviation angle" for α to avoid confusion with inclined faults. A pure shear rupture is given by $\alpha = 0°$, $\alpha = -90°$ indicates pure compression, and $\alpha = +90°$ is a pure tensile event. We use the term hybrid earthquake to distinguish faults that contain both a shear and a tensile/compressive component from pure end members. Details of the shear and tensile source models are included in Appendix 1.

FOCAL MECHANISM ANALYSIS IN HYDRAULIC INJECTIONS

We present a method for determining the geomechanical conditions for microseismic activation during hydraulic fracturing. The approach is to combine multi-array microseismic data, recorded microearthquake focal mechanisms (Stein and Wysession, 2003), and concepts of 3-D stress analysis (Jaeger et al., 2007) and stress inversion (Angelier, 1984; Reches, 1987). Integration of these techniques is well established in the structural geological and seismological communities, beginning with Anderson (1942), Wallace (1951), and Bott (1959) as a way to understand the active state of stress during faulting and seismicity (e.g., Brune, 1970; Angelier, 1984; Barth et al., 2008). Focal mechanism analysis has been used in mining, geothermal, civil engineering, and petroleum industry applications to assess geomechanical behavior during hydraulic injections, notably in the geothermal industry (Pearson, 1981; Jupe et al., 1992; Feng and Lees, 1998; Sasaki, 1998). Though microseismicity is widely used in the petroleum industry, applications are typically limited to mapping the extents of the stimulated rock volume and growth trends. This is in part related to logistical difficulties and the high cost of obtaining robust multi-array data from subsurface operations. Nonetheless, a recent emergence of petroleum industry applications has focused on hydrofracture mapping and interpretation combined with advanced applications in microseismic moment tensor and focal mechanisms analysis (Nolen-Hoeksema and

Ruff, 2001; Rutledge et al., 2004; Baig and Urbancic, 2010). Most recently, methods were presented for using stress inversion on microseismic event data to condition permeability models for reservoir simulation (Williams-Stroud and Eisner, 2010; Williams-Stroud et al., 2012a, b).

ANALYSIS METHOD

Acquiring the required source parameter and focal mechanism data used in the study entails multiple microseismic monitoring arrays or a network of geophones, detailed picking of *P*- and *S*-wave arrivals for each event, and multi-well inversion solutions to locate events and to derive the full six-component seismic moment tensors, which are decomposed to provide a range of source parameters. We investigate focal planes derived using both double-couple and tensile source model methods (Vavryčuk, 2001, 2011) (Appendix 1). We then apply a stress inversion technique that resolves the state of stress associated with slip along a collection of faults (Figure 3) (Reches, 1987), or equivalently, determines the seismotectonic regime based on the focal mechanisms of earthquakes (Angelier, 2002). We use the inversion technique of Reches (1987) because of its straightforward mechanical derivation. Implementation requires relatively few linear algebraic operations, which can be solved using MATLAB (available at http://www.mathworks.com/products/matlab/). The stress inversion technique is described in Appendix 2. Note that we prefer to reserve the terminology shear (or double-couple) model and tensile model in reference to prior nomenclature used to distinguish earthquake source models. We generally prefer the terms dilatant, contractional, shear, or hybrid (or mixed-mode) to describe the physical mechanism of the fault motion (Figure 1), whereas tensile, compressional, or shear describe the acting stress.

Data Set

In 2010, ConocoPhillips acquired microseismic data from two adjacent horizontal wells in the Barnett Shale (Figure 4). The wells were fractured in 18 sequential stages over 10 days of pumping, using a staggered toe-to-heel approach, for example, well 1 stage 1 followed by well 2 stage 1, and so forth (toe represents maximum measured depth, or maximum length along the well path). A typical stage lasted 2.5 hours at a pumping rate of 100 barrels per minute using slickwater. Microseismic events were recorded from two vertical monitor wells with 40 downhole receivers in each well (Figure 4). A contractor (Magnitude, Baker Hughes) was used to generate the velocity model, pick and locate events, and construct the six-component moment tensors. The present analysis uses the vendor-provided events locations and moment tensors. The moment-tensor decomposition and all subsequent parameters used in this study were done by the authors. We recognize that considerable uncertainty is involved in the processing of microseismic data, a fact that has led some researchers to use probabilistic analysis methods (e.g., Lund and Slunga, 1999). An independent analysis of the processing techniques used on the

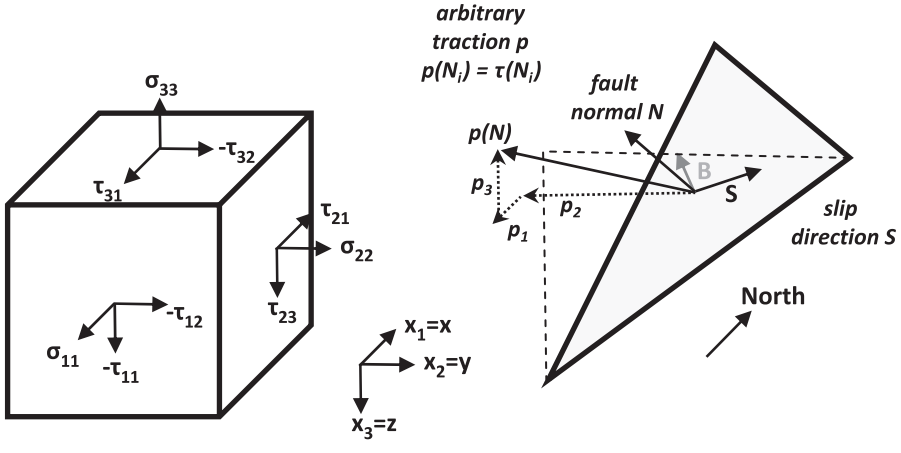

Figure 3. Stress conventions used for tensor (left) and surface (right) solutions. Compression is negative and tension is positive.

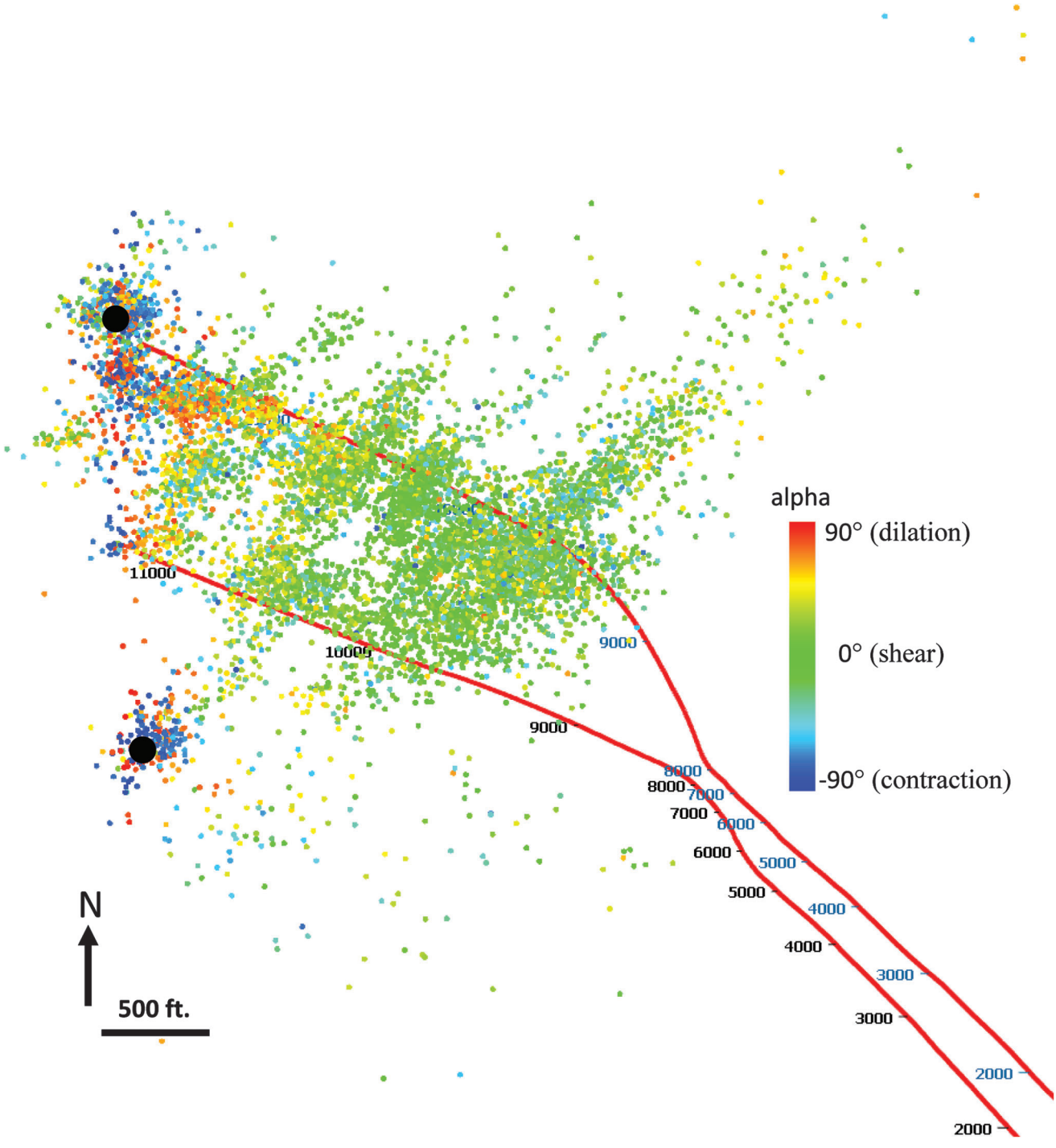

Figure 4. Map view for all 7444 Barnett Shale microseismic events used in the study. The toe of the wells is on the left and corresponds to the first injection stages. The vertical portion of the wells is on the lower right. Scale shown along the wellbores is measured depth in feet. The two monitoring wells are indicated by the black dots. Event color indicates the inclination angle α.

current data set was performed by ConocoPhillips. The largest condition numbers (e.g., Grechka and Tsvankin, 2003), a parameter that describes the uniqueness of the moment-tensor inversions, are around an order of two in the narrow area along the two geophone arrays, which is consistent with the condition numbers calculated for the actual field settings of ConocoPhillips' other unconventional resource plays. Condition numbers around orders 2–3 are several orders smaller than many other published

geophysical inversions, or at least as good as some of the most recent ones (Grechka and Tsvankin, 2003; Grechka and Yaskevich, 2014). We believe that the present moment-tensor solutions are reasonably good to serve as an example data set for us to show the methodology and analyses we developed. For details on the moment-tensor inversion and quality control metrics for this data set, such as condition number, we direct the reader to Jaio et al. (2014) (also see Du and Warpinski, 2011; Eaton and Forouhideh, 2011).

Fault-Plane Selection Criteria

The process of selecting the fault planes involves the following steps.

1. Filtering out low-confidence events based on waveform quality, noise indicators, and accuracy in event location. This step was performed by the vendor. In total, 7444 data points were selected for detailed analysis after filtering for data quality.
2. Determination of the two focal planes using either the shear or tensile model beginning with moment-tensor decomposition (Appendix 1).
3. We assume that the fault plane that slipped is the one that is more stressed (Appendix 2). This involves performing an initial stress-inversion calculation to facilitate choosing the correct plane, refining the data set based on the fault-plane selection criteria, and then performing the final stress inversion on only the selected fault population.

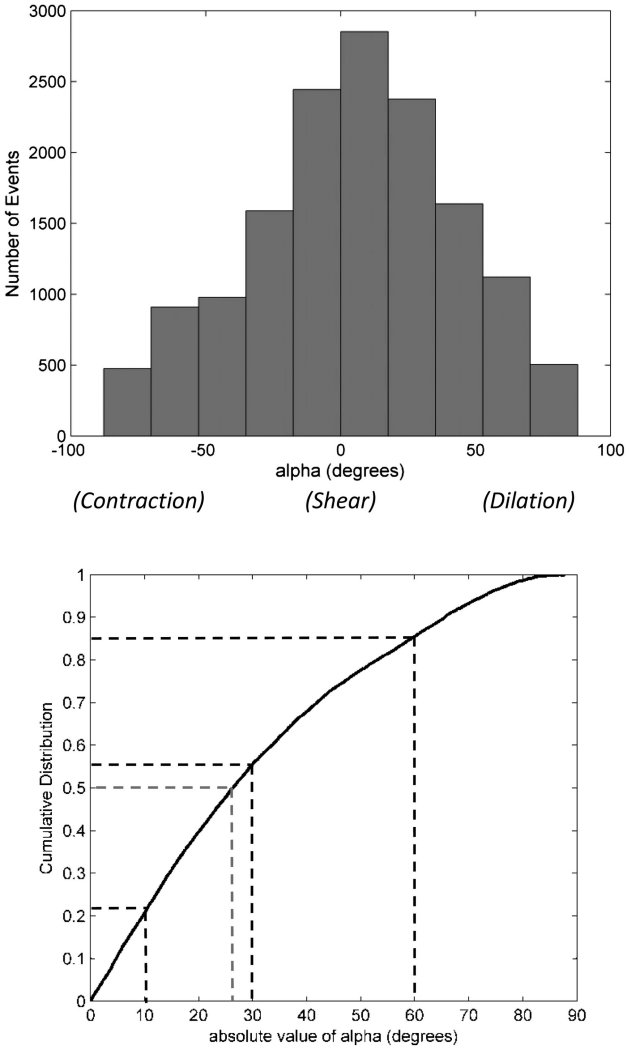

Figure 5. Distribution of deviation angle α for all events. Dashed lines indicate the 50% distribution and the distributions at $|\alpha| = 10°$, 30°, and 60°.

Computation

We implemented the above procedure in a few MATLAB algorithms in the following main steps:

1. Solving for source parameters, radiation patterns, and focal mechanisms for all events. Though we solved for a variety of source parameters (e.g., following Vavryčuk, 2001, 2011), here we focus the discussion on deviation angle α and focal plane determination.
2. Calculating the N, S, and B vectors for each plane (Figure 3; Appendix 1).
3. Implementing the coefficient of friction μ and cohesion C here with default values of $\mu = 0.6$ and $C = 0$. A parametric study of friction is included in part 2 (Busetti and Reches, 2014, this issue). Very low friction angle suggests weak, fully lubricated faults, or mixed tensile–shear motion. On the other hand, very high friction angle may be appropriate for intact rock or segmented-fault surfaces.
4. Performing an initial stress inversion (Appendix 2) for either the full focal plane population or by subpopulations. The process involves calculating the coefficients of matrix A (Appendix 2, equation 12) and vector F (Appendix 2, equation 14), then solving the system $A \times D = F$, in which D is the vector of unknown stresses, to find the unknown stresses.

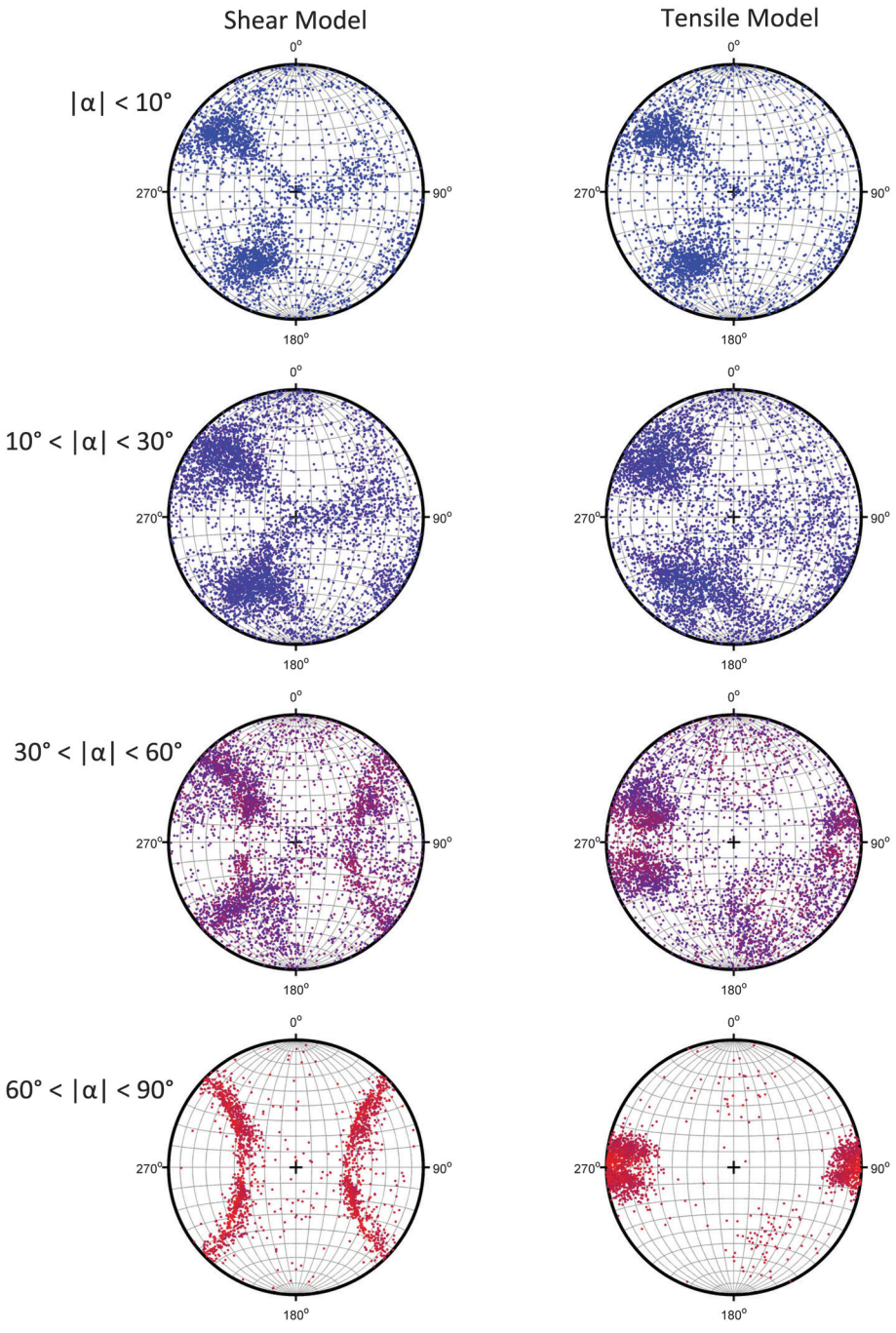

Figure 6. Focal plane orientations for all events as a function of inclination angle α. Both focal planes are shown. The left column is for planes solved using the shear model, the right is using the tensile model. Blue indicates |α| approaching 0°, red is |α| approaching 90°.

5. Solving for the tractions on each focal plane under the calculated state of stress from the initial stress inversion to facilitate fault-plane selection (Figure 3; Appendix 2).
6. Calculating instability parameters for each focal plane by manipulation of equation 6, Appendix 2. We used the critical pore (or fluid) pressure required to fail ($P_{critical}$). For each microseismic event, the true fault is selected from the two focal planes as the one with the highest value of $P_{critical}$. The value of $P_{critical}$ indicates the horizontal distance from a point on a Mohr plot to the shear failure line and can be imagined as the fluid or pore pressure to move Mohr circles leftward until fault activation occurs.
7. Repeating steps 4–6 for only the selected fault planes (Figures 5–7) to determine the activation stress state, defined as the state of stress

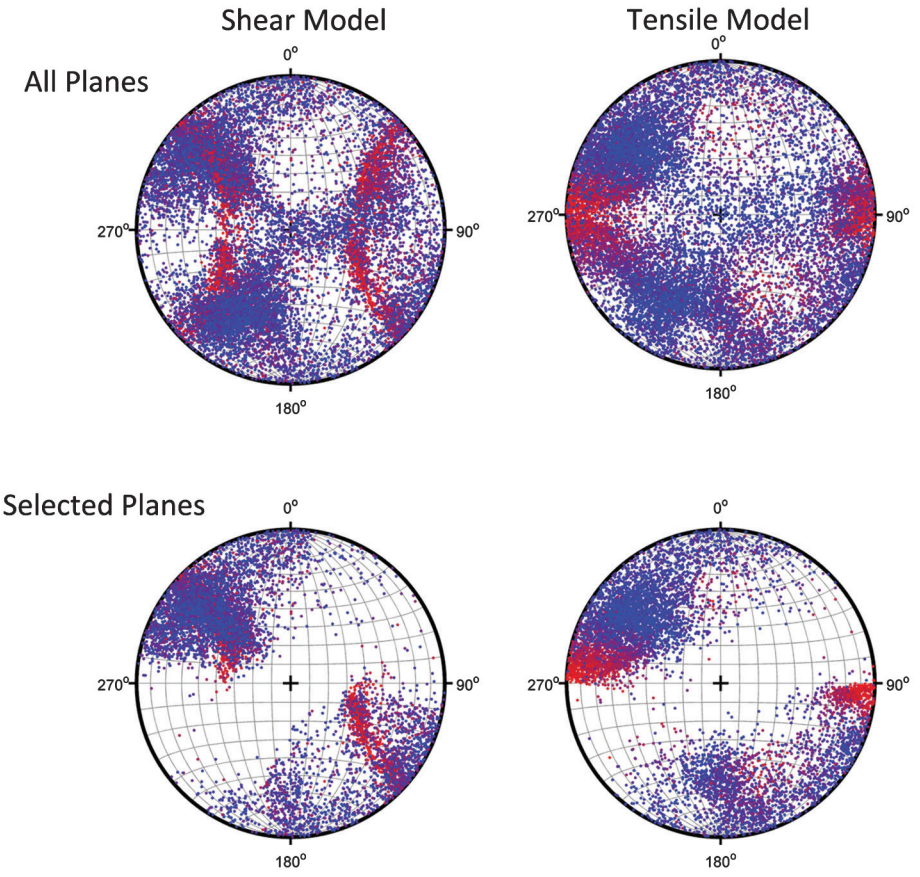

Figure 7. Focal plane orientations for all events as a function of inclination angle α. Both focal planes are shown on the top row, the selected faults are plotted on the bottom row. The left column is for planes solved using the shear model, the right is using the tensile model. Blue indicates |α| approaching 0°, red is |α| approaching 90°.

responsible for triggering or inducing the microseismic events. The stress results are listed in Table 1 and also displayed on stereonets (following Jolly and Sanderson, 1997; Zoback et al., 2012; Leclere and Fabbri, 2013) in Figures 8–10.

Note that the calculations and Table 1 use the continuum mechanics convention of compression = negative; however, for plotting purposes the stereonets display compression = positive.

RESULTS

Orientation of Microseismic Faults

We used the steps described above to determine deviation angle α and pick microseismic fault orientations for 7444 events from the two horizontal Barnett Shale wells (Figure 4). The data were broken into subgroups of $|\alpha| < 10°$, $10° < |\alpha| < 30°$, $30° < |\alpha| < 60°$, and $60° < |\alpha| < 90°$, in which |α| is the absolute value of α. Note, in part 2 (Busetti and Reches, 2014, this issue) we investigate other subsets of data such as by fracturing stage and distance to the wellbore. Nearly all the events are categorized as hybrid earthquakes, having mixed shear and tensile components (Figure 5), although shear is the dominant motion. About 75% of the events indicate |α| less than 45°. Figure 6 displays the results for all the focal planes determined in the shear and tensile models, plotted in lower hemisphere stereonet view. For $|\alpha|<10°$ the focal plane orientations are nearly identical, with two dominant inclined fault sets oriented northeast–southwest and northwest–southeast. With increasing deviation angle ($10° < |\alpha| < 30°$) small orientation differences between the two source models become visually evident, and the tensile model shows more scatter in orientation, but the general trends are similar. However, for microseismic events with higher deviation angles of $|\alpha| > 30°$, the models show severe difference of up to 45°

Table 1. Stress Inversion Results

		Stress Tensor (MPa)			Stress Direction (Eigenvectors)				Stress Path Variable	
Model	Alpha	σ_{i1}	σ_{i2}	σ_{i3}	$\sigma_{1\text{-vec}}$	$\sigma_{2\text{-vec}}$	$\sigma_{3\text{-vec}}$	AZ S_{Hmax}	p'	q
Shear	$\lvert\alpha\rvert < 10°$	−6.4	3.9	3.1	−0.15	−0.48	0.86	119.4	−15.7	17.0
		3.9	−10.5	−2.9	0.17	0.85	0.50			
		3.1	−2.9	−30.1	0.97	−0.22	0.05			
Tensile	$\lvert\alpha\rvert < 10°$	−7.2	3.3	3.3	−0.16	−0.42	0.90	115.3	−16.3	16.3
		3.3	−11.7	−3.1	0.18	0.88	0.44			
		3.3	−3.1	−30.1	0.97	−0.23	0.06			
Shear	$30° < \lvert\alpha\rvert < 10°$	−6.7	4.6	3.5	−0.16	−0.60	0.79	127.3	−15.1	17.4
		4.6	−8.5	−0.8	0.07	0.79	0.61			
		3.5	−0.8	−30.0	0.99	−0.15	0.08			
Tensile	$30° < \lvert\alpha\rvert < 10°$	−12.4	0.0	4.0	−0.20	0.15	−0.97	81.0	−20.5	12.6
		0.0	−18.9	−3.2	0.24	0.97	0.10			
		4.0	−3.2	−30.0	0.95	−0.21	−0.23			
Shear	$60° < \lvert\alpha\rvert < 30°$	−7.1	3.8	5.1	−0.21	0.41	0.89	114.1	−16.7	16.6
		3.8	−12.9	1.0	−0.01	−0.91	0.41			
		5.1	1.0	−30.0	0.98	0.07	0.19			
Tensile	$60° < \lvert\alpha\rvert < 30°$	−18.0	−5.5	5.1	−0.13	0.52	−0.85	56.6	−25.2	12.8
		−5.5	−27.6	−3.5	0.47	0.78	0.41			
		5.1	−3.5	−30.0	0.88	−0.34	−0.34			
Shear	$90° < \lvert\alpha\rvert < 60°$	−12.7	−3.5	3.9	−0.22	0.28	0.93	71.1	−20.7	15.5
		−3.5	−19.3	7.6	−0.46	0.81	−0.35			
		3.9	7.6	−30.0	0.86	0.51	0.05			
Tensile	$90° < \lvert\alpha\rvert < 60°$	−22.7	−23.1	13.0	−0.61	0.19	0.76	68.0	−26.6	34.1
		−23.1	−27.2	7.8	−0.62	0.48	−0.62			
		13.0	7.8	−30.0	0.49	0.86	0.17			
Shear	All Faults	−6.7	4.0	3.4	−0.15	−0.45	−0.88	116.7	−16.2	16.3
		4.0	−11.8	−0.1	0.04	0.89	−0.46			
		3.4	−0.1	−30.0	0.99	−0.10	−0.12			
Tensile	All Faults	−13.8	−2.8	3.5	−0.07	0.38	−0.92	64.5	−23.1	13.3
		−2.8	−25.6	−5.2	0.53	0.80	0.29			
		3.5	−5.2	−30.0	0.85	−0.46	−0.26			

(Figure 6). This difference occurs because, for the tensile source model (Appendix 1), the fault planes need to be directly corrected by the value of α. Specifically, the fault normal and slip vector are separated by 90°− α, and the angles between the fault normal and the P and T axes (referred to as the compression and tension axes, respectively) is 45°± α/2 (see figure 5 in Vavryčuk, 2001). The result of including the tensile correction is that the girdle of inclined microseismic faults (Figure 6, lower left stereonets) is resolved as a steeply dipping north–south (~010°) set of faults (Figure 6, lower right stereonets). Figure 7 plots the overall results in stereonet view and compares the undifferentiated focal planes with the selected fault planes. The selected fault planes are those most stressed under the stress state determined by an initial stress inversion (steps 4–6 above, and Appendix 2). For both models, the northwest–southeast set is rejected, and the inclined northeast–southwest fault set is dominant, corresponding to microseismic events with $\lvert\alpha\rvert < 30°$. The tensile model also maintains the steeply dipping north–south faults, which correspond to $\lvert\alpha\rvert > 30°$.

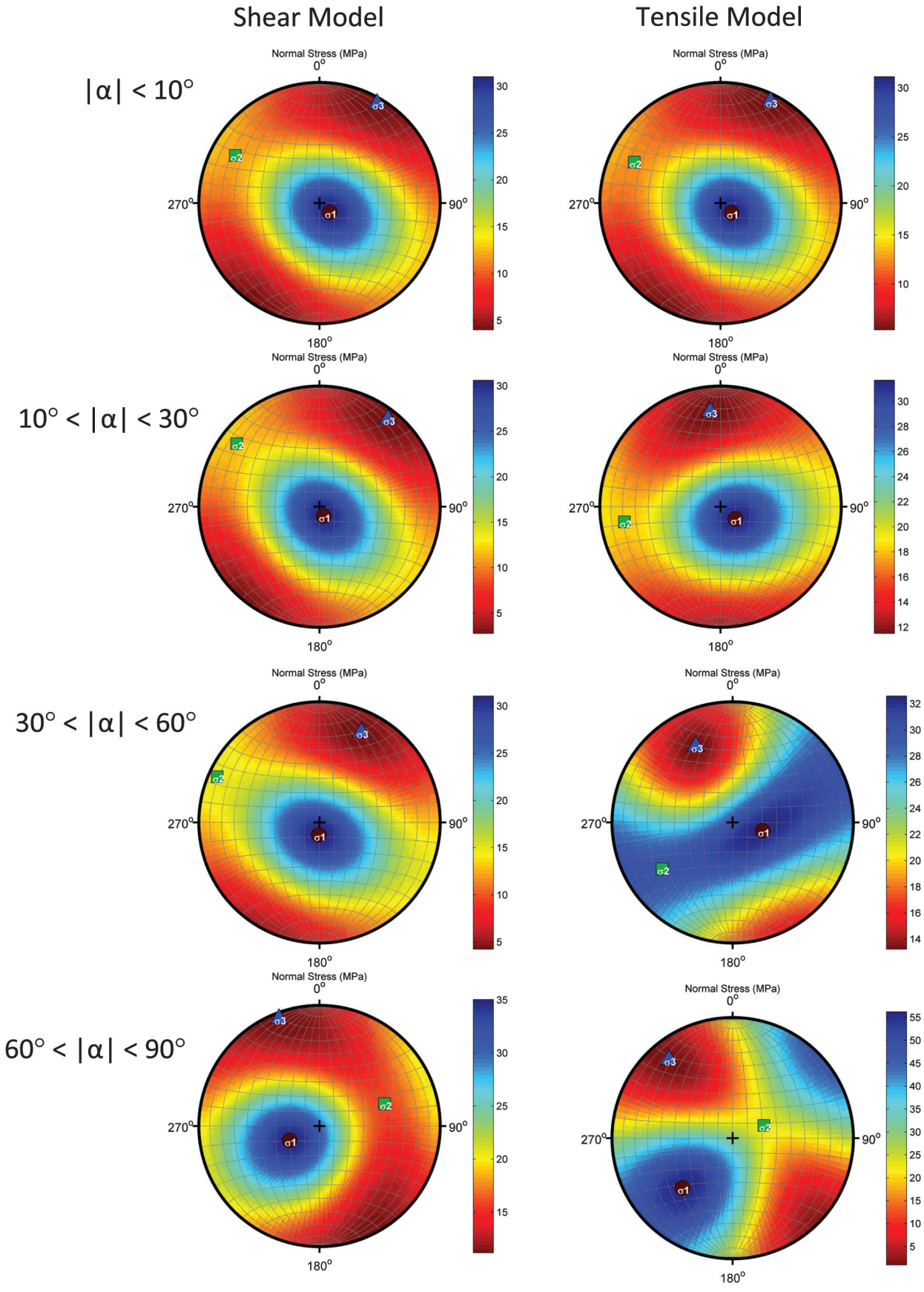
Shear Model
Tensile Model
|α| < 10°
10° < |α| < 30°
30° < |α| < 60°
60° < |α| < 90°
Normal Stress (MPa)
0°
90°
180°
270°
σ1
σ2
σ3

Stress Inversion for Microseismic Faults

To determine the microseismic activation stress state, a set of final stress inversions were run. This was done for the four subpopulations and for both the shear and tensile model-picked fault planes, for 10 independent second-stress inversions. Table 1 lists the results: components of the stress tensor σ_{ij}, the eigenvectors corresponding to the principal stress axes, in which σ_1, σ_2, and σ_3 are the principal stresses, the azimuth of the maximum horizontal stress S_{Hmax}, as well as two stress-path parameters p' and q, which are the pressure and deviatoric stress that are defined as

$$p' = 1/3(\sigma_1 + \sigma_2 + \sigma_3)$$

$$q = (1/2[\sigma_1 - \sigma_3]^2 + 1/2[\sigma_2 - \sigma_3]^2 + 1/2[\sigma_1 - \sigma_2]^2)^{1/2}$$

The activation stress state and the instability are also plotted in stereonet view in Figures 8–10. Normal stress and $P_{critical}$ were solved for all possible fault orientations from $0° \leq$ strike $\leq 360°$ and $0° \leq$ dip $\leq 90°$, plotted as poles to planes in lower hemisphere stereonet view (Figures 8–10). Each fault point is colored by its normal stress (Figure 8; top row Figure 10) or by its $P_{critical}$ (Figure 9; bottom row Figure 10) value. The principal stress axes are also plotted as symbols in each figure. The critical stress plots indicate orientations of individual faults whereby the activation stress state for that subpopulation exceeds the shear criteria (red = critically stressed or more unstable), or require reduced σ_3 to slip (blue = more stable).

As with fault orientations (Figure 6), the differences between the stress results for the shear and tensile models occur for $|\alpha| > 10°$. Table 1 and Figures 8–9 show that, whereas S_{Hmax} orientation and p' and q are very similar for the two models for microseismic events with $|\alpha| < 10°$, all of the other α subdivisions give quite different stress results. For each subdivision and for the whole population the shear model yields an S_{Hmax} azimuth that is greater than the tensile model, pressure stress p' that is lower than the tensile model, and except for the case of $30° > |\alpha| > 60°$, deviatoric stress q for the shear model that is higher than the tensile model. This discrepancy between results for the two models can be summarized by inspecting stress inversion run on the entire population of microseismic faults. The shear source model results in an activation S_{Hmax} of 116.7° versus 064.5° using the tensile model; p' is −16.2 MPa (−2350 psi) for the shear model versus −23.1 MPa (−3350 psi) for the tensile model; and q is 16.3 MPa (2364 psi) for the shear model versus 13.3 MPa (1929 psi) for the tensile model. With higher deviatoric stress and lower mean stress, the tensile model indicates the microseismic activation stress to be more failure prone than that of the shear model (e.g., on a Mohr diagram a bigger Mohr circle that is shifted leftward). The tensile model also gives S_{Hmax} that is generally more aligned with the northwest–southeast S_{Hmax} trend observed throughout the Barnett, as well as the overall trend of the microseismic event clouds (Figure 4).

DISCUSSION

Selection of the Fault Plane

A rational geomechanical workflow for differentiating the fault and auxiliary planes from microseismic focal mechanisms was described in this paper. We ran a first stress inversion on all the focal planes and selected the correct fault plane as the most unstable plane of each focal pair within the solved preliminary activation stress state. We then ran a second stress inversion on the selected planes to determine the final activation stress state. Uncertainty remains as to how to confirm, first, whether fault orientations predicted by microseismic focal solutions are accurate, and, second, whether they reflect natural fracture or fault trends. In part 2 (Busetti and Reches, 2014, this issue) we discuss

Figure 8. Calculated normal stress from stress inversion of each microseismic event subpopulation. The left column is for planes solved using the shear model, the right is using the tensile model. Blue indicates increasing compression. Note the scale bars are different.

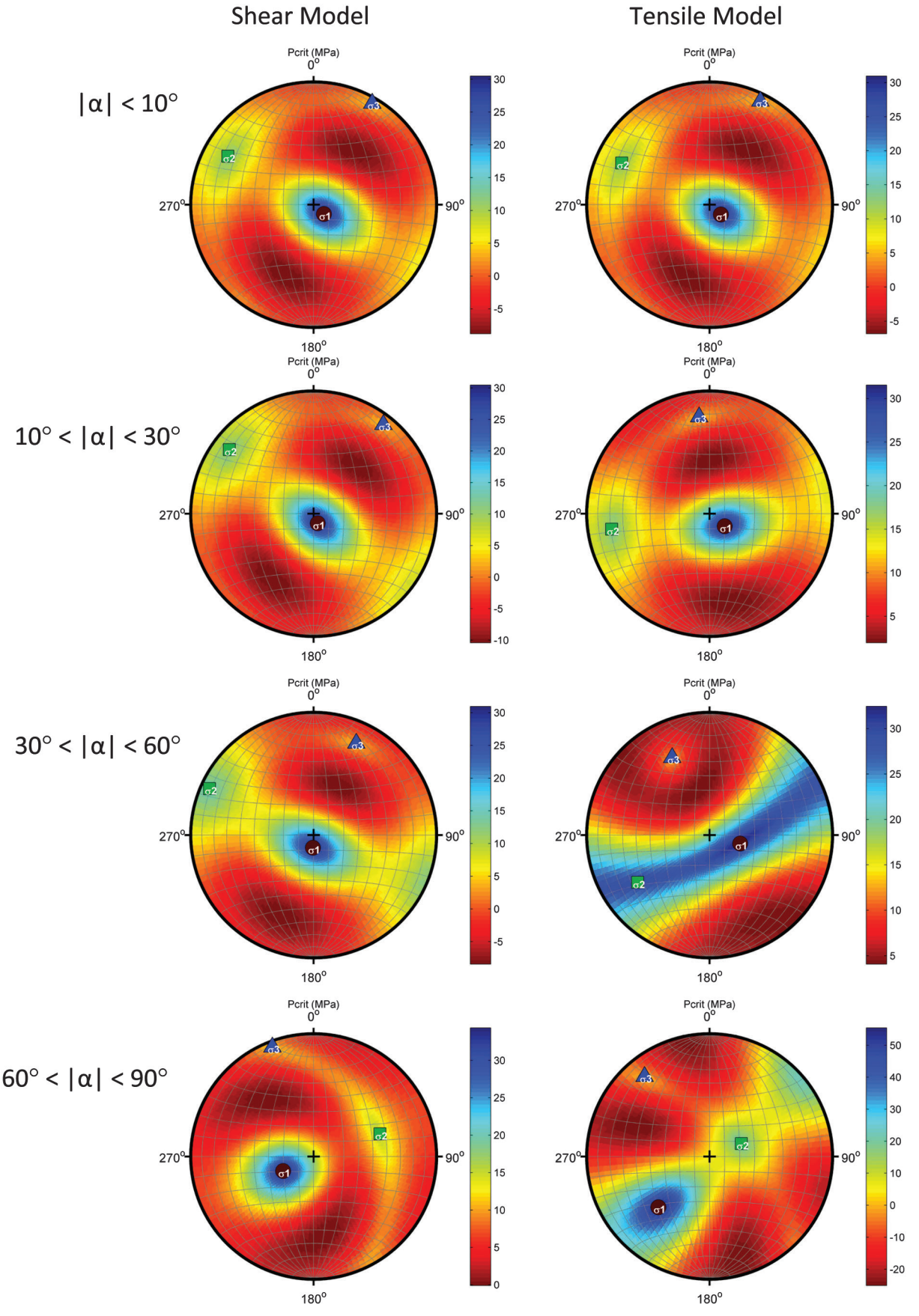
Shear Model
Tensile Model
|α| < 10°
10° < |α| < 30°
30° < |α| < 60°
60° < |α| < 90°
Pcrit (MPa)
0°
90°
180°
270°
σ1
σ2
σ3

some of the geologic trends; however, it is sufficient here to note that whereas the derived microseismic fault orientations are not incompatible with the geologic trends, from available field data no definitive way exists to confirm the orientations. For microseisms with higher values of $|\alpha|$ the tensile model successfully corrected the non-geologic girdle-like orientation pattern (lower left plots of Figure 6) and resolved a steeply dipping north–south set of fault planes, which were not detected by the shear model. Overall, the tensile model seems more representative, and we would opt to use it when the data are available and of sufficient quality.

In focusing on the geomechanical analysis techniques, we provided only minimal discussion on the accuracy of the moment data. Whether the moment-tensor data are accurate is a nontrivial problem, but it is outside the scope of the present study. Nonetheless, it cannot be understated that uncertainty in the moment tensor directly leads to uncertainty in the focal planes and their slip vectors, which in turn will affect the stress solutions, and thus ultimately cannot be downplayed.

Significance of Hybrid Events

Mechanisms for nonparallel or hybrid fault slip typically have been attributed to shear dilatancy, which is mathematically represented as a fault constitutive property, explained as either a change in friction angle for solid rock, or for discontinuous rock the result of dynamically evolving fault-surface roughness. For example, in laboratory experiments of originally undeformed rock (e.g., Ramsey and Chester, 2004), hybrid failure was associated with the transition of the yield surface from shear to tensile strength with reduction in mean and differential stress, corresponding to a rapid increase in the internal angle of friction near zero confinement. Mechanisms for hybrid failure along evolving surfaces include wear of surface asperities (e.g., Reches and Lockner, 2010) and translation along locally bumpy fault surfaces (e.g., Sagy and Brodsky, 2007). A model for hybrid failure of layered rocks was given by Ferrill and Morris (2003) to explain fault dilatancy in sedimentary rocks at depths greater than 1 km (3280 ft). They examined faulted sequences in outcrop and concluded that changes in friction angle or failure mode related to lithologic differences caused fault refraction, or changes in the orientation of otherwise continuous faults at layer interfaces. They associated hybrid failure with observations of fault dilation and enhanced fluid flow along faults. Not all of these mechanisms may be equally important during injection-induced microseismicity because of very small slip distances and short rupture times associated with the microseismic events. An alternate hydromechanical mechanism for hybrid earthquakes induced during hydraulic fracturing is fluid movement along the fault or fracture surfaces. In this case, the hybrid microseisms are caused by triggered fault slip preceding and facilitating sustained flow, or related to dynamic pressure pulses (e.g., a source of opening vs. closing events). The latter results in patterns of fluid redistribution coupled to triggered seismicity, for example, as in the fault-valve earthquake-swarm model of Sibson (1996).

The significance of the sign of α is not fully understood. However, the fact that positive and negative α events occur both near the wellbore and distally (red and blue dots in Figure 4) does reject a few hypotheses: (1) opening events occur near the wellbore where fluid pressure is highest, whereas closing events occur into the formation where tectonic stresses are more influential; (2) closing events occur near the wellbore related to near-wellbore interference and overlapping stress shadows; or similarly, (3) closing events occur near the wellbore and late in time as a result of deflation/collapse. None of these hypotheses appear to be systematically valid for the present data set. The proximity of high $|\alpha|$ events to the two monitor wells is an interesting exception and requires more rigorous synthesis of the engineering data for those wells, so is a matter for further

Figure 9. Calculated instability parameter $P_{critical}$ determined from stress inversion of each microseismic event subpopulation. The left column is for planes solved using the shear model, the right is using the tensile model. Blue indicates more stable fault orientations. Note the scale bars are different.

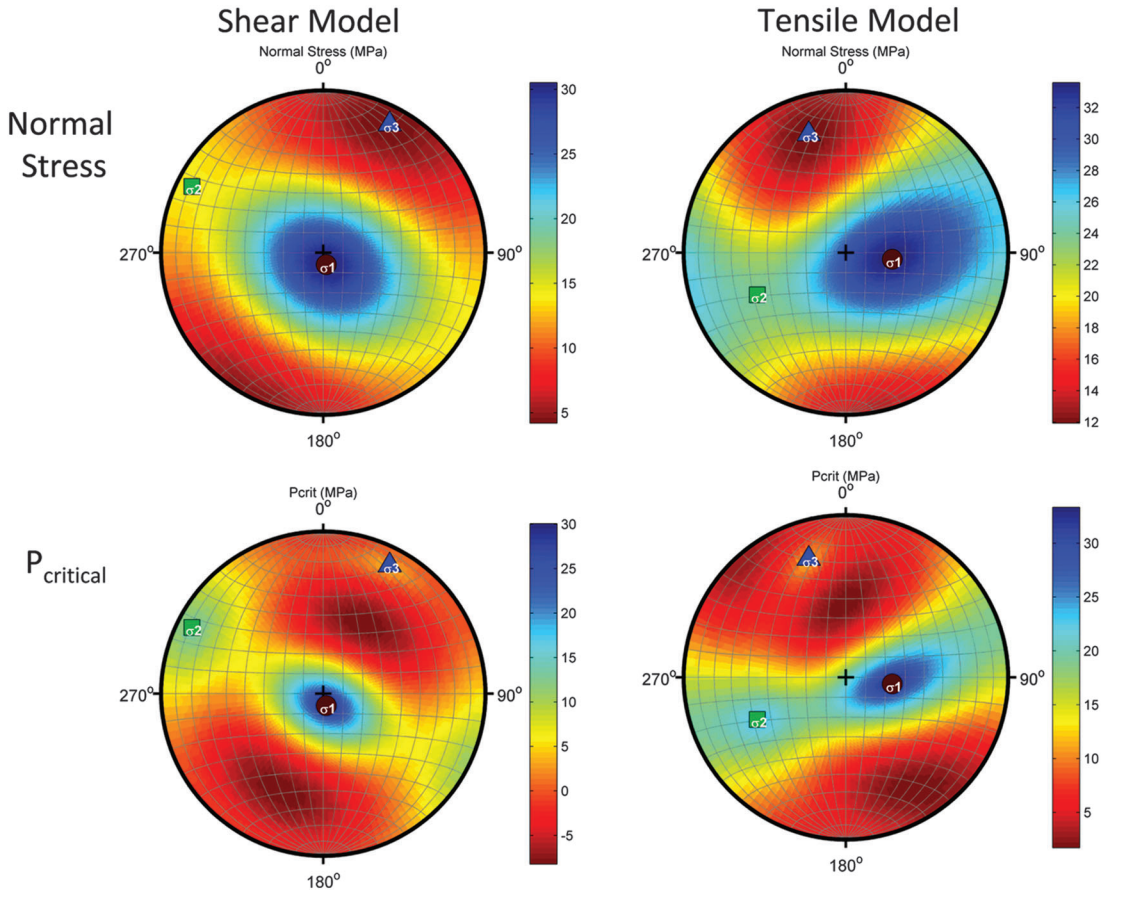

Figure 10. Normal stress and instability parameter $P_{critical}$ determined from stress inversion of the entire microseismic event population. The left column is for planes solved using the shear model, the right is using the tensile model. Note the scale bars are different.

investigation. We also viewed the microseismic data several ways: colored by α (Figure 4), colored by sequence (part 2), colored by other source parameters, grouped by stages (part 2), grouped by subsets, and so forth. Separating the events into a group for positive values of α and another for negative values of α, and then by event sequence revealed a seemingly significant result that opening and closing events overlap spatially (that is, they do not segregate into clusters by sign of α). However, they do group in time, generally extending away from the wellbore, which indicates that both opening and closing microseismic mechanisms are active during hydrofracturing and are coeval processes.

In the present Barnett Shale data set, many of the microseismic faults are aligned with the general trend of S_{Hmax}, but because the fault planes are inclined, and they have relatively low $|\alpha|$, we interpret them as pre-existing normal faults that were hydromechanically linked during injection. The microseismic faults that have the highest deviation angle ($|\alpha| > 60°$) are dominantly vertical and oriented north–south if the tensile source model is used. Without supporting stress inversion results, one might interpret these high $|\alpha|$ events to be somehow directly related to opening or closing tensile hydraulic fracture planes. However, this interpretation is inconsistent with the expected propagation directions for tensile hydraulic fractures (assuming alignment with the patterns of Figure 6). Stress inversion calculates the activation stress S_{Hmax} orientation for the $|\alpha| > 60°$ events to be 068°. Thus, we interpret these as a hydromechanically activated set of preexisting high-angle north–south faults that were present

through the stimulation area, but were either preferentially distributed or preferentially activated near the toes of the wells.

This study identified that hybrid earthquakes formed under altered activation stress states relative to the pure shear events that is a direct result of corrections made to the fault-plane orientations. For both the initial and final stress inversions, we assumed a constant friction value of $\mu = 0.6$. It is unclear if shear properties such as friction coefficient are also different for hybrid microseismic events. Although it is known that friction varies by clay content and rock rheology, laboratory-derived sliding friction values are usually determined on dry samples, and the validity of using them when modeling microseismic activation during hydraulic stimulation has yet to be determined.

CONCLUSION

In part 1 we analyzed focal mechanisms from a robust Barnett Shale microseismic data set. An iterative stress inversion technique was developed to facilitate selection of the fault plane from the auxiliary plane to characterize the microseismic fault population. We found that a tensile (or hybrid) source model is required to solve for focal plane orientations for events the moment tensors for which deviate from pure double couple. The product of correcting for the deviation angle alpha and objectively selecting the fault-plane population is a more robust and geologically relevant fault population, which is suitable for further data interpretation. In part 2 (Busetti and Reches, 2014, this issue) we compare the microseismic-derived faults with geologic data from the field, including wellbore fracture orientations. Results of the first part are used to investigate the sources of geologic heterogeneity and how that might relate to geomechanical (stress) and microseismic heterogeneity. We analyze stage-by-stage subpopulations and the role of friction. A main objective of part 2 is to expand the techniques presented here to investigate how the microseismic events relate to the hydrofractures, including whether the microseismic events are explained by hydrofracture leakoff or deformation halos.

APPENDIX 1: FOCAL MECHANISM AND SOURCE PARAMETER DETERMINATION

The analysis begins by performing decomposition of the six-component moment tensor $\mathbf{M}$ for each microseismic event (Vavryčuk, 2001), in which $\mathbf{M_{ij}}$ is the 3×3 seismic moment tensor.

$$\mathbf{M} = \begin{bmatrix} M_{xx} & M_{xy} & M_{xz} \\ M_{yx} & M_{yy} & M_{yz} \\ M_{zx} & M_{zy} & M_{zz} \end{bmatrix} \tag{1a}$$

$$\mathbf{M} = \mathbf{M}^{\mathrm{ISO}} + \mathbf{M}^{\mathrm{CLVD}} + \mathbf{M}^{\mathrm{DC}} \tag{1b}$$

$$m_j = \begin{bmatrix} m_1 & 0 & 0 \\ 0 & m_2 & 0 \\ 0 & 0 & m_3 \end{bmatrix} \qquad (m_1 \geq m_2 \geq m_3) \tag{1c}$$

The right side of (1b) gives the isotropic, compensated linear vector dipole, and double-couple components of $\mathbf{M}$. In terms of its principal coordinate, the tensor is given by its eigenvalues as m_j in (1c). The most compressive, least compressive, and intermediate eigenvalues of $\mathbf{M}$ correspond to the P, T, and null axes, which are mutually perpendicular and directional components for which are given by the eigenvectors of $\mathbf{M}$. A right-hand convention is used in which X+ is north, Y+ is east, and Z+ is down. Assuming a shear source, the unit normal vector for each plane $\mathbf{N}$ bisects the P and T axes at an angle of 45°. The T axis bisects $\mathbf{N}$ and the slip vector on the plane $\mathbf{S}$, so that $\mathbf{N}$ and $\mathbf{S}$ are readily determined from $\mathbf{M}$ (Figure 3). If the source is not a pure double couple, then the angle from P or T to $\mathbf{N}$ must be modified by $\pm\alpha/2$, in which α is the deviation angle.

We follow the approach of Vavryčuk (2001) in performing the decomposition of $\mathbf{M}$ for moment tensors with a tensile component to the source. The deviatoric component of the moment tensor, m_j', is the difference between m_j, the eigenvalues of $\mathbf{M}$, and the volumetric component $\mathbf{M^{ISO}}$, equal to $tr(m)/3$ (e.g., Aki and Richards, 1980):

$$\begin{bmatrix} m_1' & 0 & 0 \\ 0 & m_2' & 0 \\ 0 & 0 & m_3' \end{bmatrix} = \begin{bmatrix} m_1 & 0 & 0 \\ 0 & m_2 & 0 \\ 0 & 0 & m_3 \end{bmatrix} - \begin{bmatrix} \frac{tr(m)}{3} & 0 & 0 \\ 0 & \frac{tr(m)}{3} & 0 \\ 0 & 0 & \frac{tr(m)}{3} \end{bmatrix} \tag{2}$$

in which $j = 1, 2, 3$. The deviatoric component is used to determine α, the inclination of the resolved slip vector off of the plane, and is a measure of the departure from perfect double-couple (shear-slip) mechanisms, in which the sign indicates contraction or dilatancy. The deviation angle α is given by (Vavryčuk, 2001):

$$\alpha = \mathrm{asin}\left[3\frac{\max(m_j') + \min(m_j')}{|\max(m_j')| + |\min(m_j')|}\right] \tag{3}$$

The vertical brackets in the denominator terms denote absolute values. We use α only as a relative indicator of dilatancy/contraction caused by imprecision in the magnitude of the isotropic component, which we attribute to intrinsic noise in the microseismic events. The deviatoric part can further be split, corresponding to the $\mathbf{M}^{\mathrm{DC}}$ and $\mathbf{M}^{\mathrm{CLVD}}$ components in equation 1b; however, these procedures are not central to the present study.

Focal Planes from a Shear Source

The components of the moment tensor contain information on the fault geometry, whereas the size of the earthquake is indicated by the scalar moment M_0. For a double-couple (purely shear rupture) source, **M** and the fault normal and slip vectors **N** and **S** are related to M_0 as follows (Stein and Wysession, 2003):

$$\mathbf{M} = M_0(N_i S_j + N_j S_i) \tag{4a}$$

$$\mathbf{M} = M_0 \begin{bmatrix} 2N_xS_x & N_xS_y + N_yS_x & N_xS_z + N_zS_x \\ N_yS_x + N_xS_y & 2N_yS_y & N_yS_z + N_zS_x \\ N_zS_x + N_xS_z & N_zS_y + N_yS_z & 2N_zS_z \end{bmatrix} \tag{4b}$$

in which N_i and S_i are the i-th component of **N** and **S**, respectively. Understanding the relationship between N_i and S_i in equations 4a and 4b, and the symmetry ($\mathbf{M_{ij}} = \mathbf{M_{ji}}$) in equations 1a and 4b is important for subsequent geologic interpretation. The equations indicate that, from a moment-tensor solution, slip on either the fault or auxiliary plane cannot be physically differentiated using seismic data alone as they yield the same radiation patterns (Stein and Wysession, 2003). Therefore, ambiguity exists in determining fault plane and slip direction from moment-tensor solutions.

Focal Planes from a Tensile Source

Vavryčuk (2001, 2011) derived equations for the tensile source model, defined as a seismic source that occurs across a fault plane, but in which the slip direction is not constrained to be parallel to the plane. The angle between the slip direction and the fault plane, denoted as α, ranges from −90° (pure compression) to +90° (pure tensile) (Figure 5). A pure shear rupture is given by $\alpha = 0°$, which is the case for many shallow tectonic earthquakes. Considering the acoustic emissions data collected from laboratory experiments as well as microearthquake data from various fields, a process in which slip is decoupled from the fault plane is a reasonable model for the microseismic events triggered by fluid injection during hydraulic fracturing.

Let $\mathbf{e}_1$, $\mathbf{e}_2$, and $\mathbf{e}_3$ denote unit vectors in the three principal directions corresponding to m_1, m_2, and m_3, then fault normal and slip can be calculated (Vavryčuk, 2011):

$$\mathbf{N} = \sqrt{\frac{m_1 - m_2}{m_1 - m_3}}\mathbf{e}_1 + \sqrt{\frac{m_2 - m_3}{m_1 - m_3}}\mathbf{e}_3 \tag{5a}$$

$$\mathbf{S} = \sqrt{\frac{m_1 - m_2}{m_1 - m_3}}\mathbf{e}_1 - \sqrt{\frac{m_2 - m_3}{m_1 - m_3}}\mathbf{e}_3 \tag{5b}$$

As with the shear source decomposition, **N** and **S** are exchangeable for the complementary plane solutions. Not all complete moment-tensor solutions satisfy a stable tensile source model. Two obvious exceptions are pure explosion or pure implosion, in which cases no actual fault plane exists, and terms in equations 1 and 2 would be unstable because of division by zero. The principal components m_1, m_2, and m_3 must satisfy a stable condition for the source to be considered a tensile source (Vavryčuk, 2011), and to be used to determine fault and slip direction. We apply the above methods to the microseismic events data from the Barnett Shale. The shear source solution used the full data set to calculate focal planes for 7444 events. By solving for focal planes from both shear and tensile sources, we are able to assess using a more realistic source model on the geomechanical solutions.

APPENDIX 2: STRESS INVERSION TECHNIQUE

The approach is to use stress inversion techniques commonly applied to fault slip and earthquake problems (Angelier, 1984) to determine the activation stress, the local stress state required to induce microseismicity. The inversion method used here is following the technique of Reches (1987) that relies on two main assumptions:

Assumption 1: The slip along a fault occurs in the direction of maximum shear stress, or equivalently, normal to the direction of zero shear stress.
Assumption 2: The magnitudes of the shear stresses on the fault satisfy the Coulomb yield criterion:

$$|\tau| > C + \mu\sigma_n \tag{6}$$

in which $|\tau|$ is the absolute magnitude of the shear stress in the slip direction, C is cohesion, μ is the coefficient of friction, and σ_n is the normal stress on the fault. Following the procedure of Jaeger et al. (2007, chapter 2), Cauchy's formula is invoked to resolve the stresses on an arbitrary plane subjected to a local stress field, σ_{ij}. The stress inversion technique considers that if the fault cohesion, angle of friction, fault orientation, and slip direction are known, then the maximum shear stress and remaining components of the stress tensor can be calculated. The assumption that the in-plane direction corresponding with the maximum shear stress coincide with the slip direction, as well as specifying one component of the stress tensor, overburden σ_{33}, creates an overdetermined problem that can be solved using linear techniques (Michael, 1984; Reches, 1987). The other popular method, which is not used here, is based on grid-search algorithms (e.g., Gephart and Forsyth, 1984).

The unit vectors **N**, the unit normal axis **S**, the unit slip axis, and **B**, the unit axis normal to **S** on the plane (Figure 3), in which $\mathbf{B} = \mathbf{N} \times \mathbf{S}$, are known quantities for each fault plane from the moment-tensor inversion solutions, equation 4b. The traction $p(\mathbf{N})$ on a plane described by unit normal vector **N** and the unit vector representing the spatial coordinate system, $\mathbf{e}_i$, is given by

$$p(\mathbf{N}) = N_x p(\mathbf{e_x}) + N_y p(\mathbf{e_y}) + N_z p(\mathbf{e_z}) \tag{7a}$$

The components of the traction in the x, y, and z directions are:

$$p(\mathbf{e}_x) = [\,\sigma_{xx} \quad \tau_{xy} \quad \tau_{xz}\,] \tag{7b}$$

$$p(\mathbf{e}_y) = [\,\tau_{yx} \quad \sigma_{yy} \quad \tau_{yz}\,] \tag{7c}$$

$$p(\mathbf{e}_z) = [\,\tau_{zx} \quad \tau_{zy} \quad \sigma_{zz}\,] \tag{7d}$$

The directional components of the traction vector can be substituted in equation 7a and written in matrix form:

$$p(\mathbf{N}) = \begin{bmatrix} p_x(N) \\ p_y(N) \\ p_z(N) \end{bmatrix} = \begin{bmatrix} \sigma_{xx} & \tau_{xy} & \tau_{xz} \\ \tau_{yx} & \sigma_{yy} & \tau_{yz} \\ \tau_{zx} & \tau_{zy} & \sigma_{zz} \end{bmatrix} \begin{bmatrix} N_x \\ N_y \\ N_z \end{bmatrix} \quad (7e)$$

The symbols σ_{ij} and τ_{ij} are the stress components and the indices x_i reflect the coordinate system in which $x_1 = x$ points north, $x_2 = y$ points east, and $x_3 = z$ points down. The solution for planes on which the shear stresses vanish and the traction vector is parallel to the outward unit normal vector is given in the original coordinate system [1 0 0], [0 1 0], [0 0 1] by:

$$\begin{bmatrix} \sigma_{xx} - \sigma & \tau_{xy} & \tau_{xz} \\ \tau_{yx} & \sigma_{yy} - \sigma & \tau_{yz} \\ \tau_{zx} & \tau_{zy} & \sigma_{zz} - \sigma \end{bmatrix} \begin{bmatrix} N_x \\ N_y \\ N_z \end{bmatrix} = \begin{bmatrix} 0 \\ 0 \\ 0 \end{bmatrix} \quad (8)$$

in which σ is a normalizing scalar stress. For fault slip analysis, we are interested in the conditions that maximize shear stress on a plane with arbitrary orientation. This is on the plane identified with normal vector **N** and in the direction of **S**. Applying a transformation results in the following forms:

$$[S_x \quad S_y \quad S_z] \begin{bmatrix} \sigma_{xx} - \sigma & \tau_{xy} & \tau_{xz} \\ \tau_{yx} & \sigma_{yy} - \sigma & \tau_{yz} \\ \tau_{zx} & \tau_{zy} & \sigma_{zz} - \sigma \end{bmatrix} \begin{bmatrix} N_x \\ N_y \\ N_z \end{bmatrix} = 0 \quad (9a)$$

$$[B_x \quad B_y \quad B_z] \begin{bmatrix} \sigma_{xx} - \sigma & \tau_{xy} & \tau_{xz} \\ \tau_{yx} & \sigma_{yy} - \sigma & \tau_{yz} \\ \tau_{zx} & \tau_{zy} & \sigma_{zz} - \sigma \end{bmatrix} \begin{bmatrix} N_x \\ N_y \\ N_z \end{bmatrix} = 0 \quad (9b)$$

$$[N_x \quad N_y \quad N_z] \begin{bmatrix} \sigma_{xx} - \sigma & \tau_{xy} & \tau_{xz} \\ \tau_{yx} & \sigma_{yy} - \sigma & \tau_{yz} \\ \tau_{zx} & \tau_{zy} & \sigma_{zz} - \sigma \end{bmatrix} \begin{bmatrix} N_x \\ N_y \\ N_z \end{bmatrix} = 0 \quad (9c)$$

Multiplication of equation 9b, setting $\sigma = \sigma_{33}$ (normalizing by overburden), applying symmetry of $\tau_{ij} = \tau_{ji}$, and substituting indices 1, 2, and 3 for x, y, and z gives assumption 1 as:

$$\begin{aligned}(\sigma_{11} - \sigma_{33})N_1B_1 + (\sigma_{22} - \sigma_{33})N_2B_2 + \tau_{23}(N_2B_3 + N_3B_2) \\ + \tau_{13}(N_1B_3 + N_3B_1) + \tau_{12}(N_1B_2 + N_2B_1) = 0\end{aligned} \quad (10)$$

Replacing τ and σ_n in equation 6 with the product of 9a and 9b, respectively, yields:

$$\begin{aligned}&(\sigma_{11} - \sigma_{33})N_1S_1 + (\sigma_{22} - \sigma_{33})N_2S_2 + \tau_{23}(N_2S_3 + N_3S_2) \\ &\quad + \tau_{13}(N_1S_3 + N_3S_1) + \tau_{12}(N_1S_2 + N_2S_1) = C \\ &\quad + \mu[(\sigma_{11} - \sigma_{33})N_1^2 + (\sigma_{22} - \sigma_{33})N_2^2 \\ &\quad + \tau_{23}(N_2N_3 + N_3N_2) + \tau_{13}(N_1N_3 + N_3N_1) \\ &\quad + \sigma_{33} + \tau_{12}(N_1N_2 + N_2N_1)]\end{aligned} \quad (11)$$

Following Reches (1987), equations 10 and 11 form the basis for a linear system of equations given by the matrix $\mathbf{A} \times \mathbf{D} = \mathbf{F}$. Matrix **A** is a $2K \times 5$ matrix containing the information on the fault parameters, in which K is the number of faults. Equation 11 is rearranged to match the five-component form of equation 10. **D** is the vector of unknown stresses with five terms. **F** is a vector with $2K$ terms. The matrix **A** has the form:

$$\begin{bmatrix} [N_1B_1]_1 & [N_2B_2]_1 & [N_2B_3 + N_3B_2]_1 & [N_1B_3 + N_3B_1]_1 & [N_1B_2 + N_2B_1]_1 \\ \cdots & \cdots & \cdots & \cdots & \cdots \\ [N_1B_1]_k & [N_2B_2]_k & [N_2B_3 + N_3B_2]_k & [N_1B_3 + N_3B_1]_k & [N_1B_2 + N_2B_1]_1 \\ \cdots & \cdots & \cdots & \cdots & \cdots \\ [N_1S_1 - \mu N_1^2]_1 & [N_2S_2 - \mu N_2^2]_1 & [N_2S_3 + S_2N_3 - 2\mu N_2N_3]_1 & [N_1S_3 + S_1N_3 - 2\mu N_1N_3]_1 & [N_1S_2 + S_1N_2 - 2\mu N_1N_2]_1 \\ \cdots & \cdots & \cdots & \cdots & \cdots \\ [N_1S_1 - \mu N_1^2]_k & [N_2S_2 - \mu N_2^2]_k & [N_2S_3 + S_3N_3 - 2\mu N_2N_3]_k & [N_1S_3 + S_1N_3 - 2\mu N_1N_3]_k & [N_1S_2 + S_1N_2 - 2\mu N_1N_2]_k \\ \cdots & \cdots & \cdots & \cdots & \cdots \end{bmatrix} \quad (12)$$

The vector **D** of the unknown stresses has the form:

$$[(\sigma_{11} - \sigma_{33}) \quad (\sigma_{22} - \sigma_{33}) \quad \tau_{23} \quad \tau_{13} \quad \tau_{12}]^T \quad (13)$$

The vector **F** provides inputs for the parameters C, μ, and σ_{33} used in equation 11. The first K terms corresponding to equation 10 are zero, the latter terms are specified. Vector **F** has the form:

$$[0 \quad 0 \quad \cdots \quad \cdots \quad (C + \mu\sigma_{33}) \quad (C + \mu\sigma_{33}) \quad \cdots]^T \quad (14)$$

The system $\mathbf{A} \times \mathbf{D} = \mathbf{F}$ is an over-determined linear system in which **A** and **F** are known for the fault and slip orientations and μ and C are given as input values. The stress vector **D** can be determined by linear algebra methods. **D** reflects the local state of stress that satisfies the critical stress conditions in equations 10 and 11 for all K faults. Additionally, **D** can be computed for subsets of K, that is, predetermined fault orientations and/or individual hydrofracture stages.

The normal stress, maximum shear stress, and slip direction are calculated for each fault (Figure 3) by using the calculated stress tensor σ_{ij} from the stress inversion to compute the components of the traction vector on the plane (Jaeger et al., 2007, p. 31). The normal stress σ_n is the dot product of the unit normal for the fault and the traction vector (equation 7e), and the shear stress τ is solved using the Pythagorean Theorem:

$$\sigma_n = \mathbf{N} \cdot p(\mathbf{N}) \tag{15a}$$

$$\tau^2 = p(\mathbf{N})^2 - \sigma_n^2 \tag{15b}$$

Once the maximum shear stress and its direction on each fault plane are determined, the calculated slip vector can be compared with the input slip vector for each fault. Two popular approaches exist to calculate the misfit. The minimum rotation technique does not restrict the misfit angle to being in the fault plane, and the angle of rotation needed to minimize the misfit can occur on any axis. This method was used (e.g., Gephart and Forsyth, 1984) assuming the data may have both uncertainties in the correct nodal planes and slip vector orientations (Allmendinger, 1989). This study takes a more simplistic approach and assumes that the orientations of the fault planes are correct and the actual slip vector should lie within that plane. This has been referred to as the pole rotation method. The polar rotation misfit angle is calculated as follows:

$$\alpha_{misfit} = \cos^{-1}(\tau \cdot \mathbf{S}) \tag{16}$$

in which the misfit angle α_{misfit} is the angle between the unit shear stress direction τ and the unit slip direction **S**, and · indicates the dot product.

REFERENCES CITED

Aki, K., and P. G. Richards, 1980, Quantitative seismology: Theory and methods, Volume I: San Francisco, California, W.H. Freeman and Co., 557 p.

Allmendinger, R. W., 1989, Notes on fault slip analysis: Geological Society of America Short Course on Quantitative Interpretation of Joints and Faults, 1: Boulder, Colorado, Geological Society of America, 56 p.

Anderson, E. M., 1942, The dynamics of faulting: London, Oliver and Boyd, 183 p.

Angelier, J., 1984, Tectonic analysis of fault slip data sets: Journal of Geophysical Research, v. 89, p. 5835–5848, doi:10.1029/JB089iB07p05835.

Angelier, J., 2002, Inversion of earthquake focal mechanisms to obtain the seismotectonic stress IV–A new method free of choice among nodal planes: Geophysical Journal International, v. 150, no. 3, p. 588–609, doi:10.1046/j.1365-246X.2002.01713.x.

Baer, G., 1991, Mechanisms of dike propagation in layered rocks and in massive porous sedimentary rocks: Journal of Geophysical Research, v. 96, no. B7, p. 11911–11929, doi:10.1029/91JB00844.

Baig, A., and T. Urbancic, 2010, Microseismic moment tensors: A path to understanding frac growth: The Leading Edge, v. 29, no. 3, p. 320–324, doi:10.1190/1.3353729.

Barth, A., J. Reinecker, and O. Heidbach, 2008, Stress derivation from earthquake focal mechanisms: World Stress Map Project Guidelines, 12 p., accessed October 14, 2014, http://extras.springer.com/2010/978-1-4020-8443-0/WSM%20Release%202008/WSM_website/pub/guidelines/WSM_analysis_guideline_focal_mechanisms.pdf.

Bott, M. H. P., 1959, The mechanics of oblique slip faulting: Geological Magazine, v. 96, no. 2, p. 109–117, doi:10.1017/S0016756800059987.

Brune, J. N., 1970, Tectonic stress and the spectra of seismic shear waves from earthquakes: Journal of Geophysical Research, v. 75, no. 26, p. 4997–5009, doi:10.1029/JB075i026p04997.

Busetti, S., and Z. Reches, 2014, Geomechanics of hydraulic fracturing microseismicity: Part 2. Stress state determination: AAPG Bulletin, v. 98, p. 2459–2476, doi:10.1306/05141413124.

Delaney, P. T., and D. D. Pollard, 1981, Deformation of host rocks and flow of magma during growth of minette dikes and breccia-bearing intrusions near Ship Rock: New Mexico, United States Geological Survey professional paper 1202, 61 p.

Du, J., and N. Warpinski, 2011, Uncertainty in FPSs from moment-tensor inversion: Geophysics, v. 76, no. 6, p. WC65–WC75, doi:10.1190/geo2011-0024.1.

Eaton, D., and F. Forouhideh, 2011, Solid angles and the impact of receiver-array geometry on microseismic moment-tensor inversion: Geophysics, v. 76, no. 6, p. WC75–WC83, doi:10.1190/geo2011-0077.1.

Engelder, T., 1999, Transitional-tensile fracture propagation: a status report: Journal of Structural Geology, v. 21, no. 8–9, p. 1049–1055, doi:10.1016/S0191-8141(99)00023-1.

Feng, Q., and J. M. Lees, 1998, Microseismicity, stress, and fracture in the Coso geothermal field, California: Tectonophysics, v. 289, no. 1–3, p. 221–238, doi:10.1016/S0040-1951(97)00317-X.

Ferrill, D. A., R. N. McGinnis, A. P. Morris, and K. J. Smart, 2012, Hybrid failure: Field evidence and influence on fault refraction: Journal of Structural Geology, v. 42, p. 140–150, doi:10.1016/j.jsg.2012.05.012.

Ferrill, D. A., and A. P. Morris, 2003, Dilational normal faults: Journal of Structural Geology, v. 25, p. 183–196.

Gephart, J. W., and D. W. Fortsyth, 1984, An improved method for determining the regional stress tensor using earthquake focal mechanisms data: an application to the San Fernando earthquake sequence: Journal of Geophysical Research, v. 89, no. B11, p. 9305–9320, doi:10.1029/JB089iB11p09305.

Grechka, V., and I. Tsvankin, 2003, Feasibility of seismic characterization of multiple fracture sets: Geophysics, v. 68, no. 4, p. 1399–1407, doi:10.1190/1.1598133.

Grechka, V., and S. Yaskevich, 2014, Azimuthal anisotropy in microseismic monitoring: A Bakken case study: Geophysics: v. 79, no. 1, p. KS1–KS12, doi:10.1190/geo2013-0211.1.

Jaeger, J. C., N. G. W. Cook, and R. Zimmerman, 2007, Fundamentals of rock mechanics, 4th ed.: Malden, Massachusetts, Blackwell Publishing, 475 p.

Jaio, W., M. Davidson, A. Sena, B. L. Bankhead, Y. Xia, S. Sil, and C. Zhou, 2014, The matter of size: On the moment magnitude of microseismic events: Geophysics, v. 79, no. 3, p. KS31–KS41, doi:10.1190/geo2013-0194.1.

Jolly, R. J. H., and D. J. Sanderson, 1997, A Mohr circle construction for the opening of a pre-existing fracture: Journal of Structural Geology, v. 19, no. 6, p. 887–892, doi:10.1016/S0191-8141(97)00014-X.

Jupe, A. J., A. S. P. Green, and T. Wallroth, 1992, Induced microseismicity and reservoir growth at the Fjallback hot dry rocks project, Sweden: International Journal of Rock Mechanics and Mining Sciences & Geomechanics Abstracts, v. 29, no. 4, p. 343–354, doi:10.1016/0148-9062(92)90511-W.

Leclere, H., and O. Fabbri, 2013, A new three-dimensional method of fault reactivation analysis: Journal of Structural Geology, v. 48, p. 153–161, doi:10.1016/j.jsg.2012.11.004.

Lund, B., and R. Slunga, 1999, Stress tensor inversion using detailed microearthquake information and stability constraints: Application to Olfus in southwest Iceland: Journal of Geophysical Research, v. 104, no. B7, p. 14947–14964, doi:10.1029/1999JB900111.

Mandl, G., 1988, Mechanics of Tectonic Faulting: New York, Elsevier, 409 p.

Michael, A., 1984, Determination of stress from slip data: fault and folds: Journal of Geophysical Research, B, v. 89, no. B13, p. 11,517–11,526, doi:10.1029/JB089iB13p11517.

Nolen-Hoeksema, R. C., and L. J. Ruff, 2001, Moment tensor inversion of microseismic from the B-sand propped hydrofracture, M-site, Colorado: Tectonophysics, v. 336, no. 1–4, p. 163–181, doi:10.1016/S0040-1951(01)00100-7.

Pearson, C., 1981, The relationship between microseismicity and high pore pressures during hydraulic stimulation experiments in low permeability granitic rocks: Journal of Geophysical Research, v. 86, no. B9, p. 7855–7864, doi:10.1029/JB086iB09p07855.

Pollard, D. D., O. H. Muller, and D. R. Dockstader, 1975, The forma and growth of fingered sheet intrusions: Geological Society of America Bulletin, v. 86, no. 3, p. 351–363, doi:10.1130/0016-7606(1975)86<351:TFAGOF>2.0.CO;2.

Ramsey, J. M., and F. M. Chester, 2004, Hybrid fracture and the transition from extension fracture to shear fracture: Nature, v. 428, p. 63–66, doi:10.1038/nature02333.

Reches, Z., 1987, Determination of the tectonic stress tensor from slip analysis along faults that obey the coulomb yield condition: Tectonics, v. 6, no. 6, p. 849–861, doi:10.1029/TC006i006p00849.

Reches, Z., and J. Fink, 1988, The mechanism of intrusion of the Inyo dike, Long Valley Caldera, California: Journal of Geophysical Research, v. 93, no. B5, p. 4321–4334, doi:10.1029/JB093iB05p04321.

Reches, Z., and D. Lockner, 2010, Fault weakening and earthquake instability by powder lubrication: Nature, v. 467, p. 452–455, doi:10.1038/nature09348.

Rutledge, J. T., W. S. Phillips, and M. J. Mayerhofer, 2004, Faulting induced by forced fluid injection and fluid flow forced by faulting: An interpretation of hydraulic-fracture microseismicity, Carthage Cotton Valley gas field, Texas: Bulletin of the Seismological Society of America, v. 94, no. 5, p. 1817–1830, doi:10.1785/012003257.

Sagy, A., and E. Brodsky, 2007, Evolution of fault-surface roughness with slip: Geology, v. 35, no. 3, p. 283–286, doi:10.1130/G23235A.1.

Sasaki, S., 1998, Characteristics of microseismic events during hydraulic fracturing experiments at the Hijori hot dry rock geothermal energy site, Yamagata, Japan: Tectonophysics, v. 289, no. 1–3, p. 171–188, doi:10.1016/S0040-1951(97)00314-4.

Sibson, R. H., 1996, Structural permeability of fluid-driven fault-fracture meshes: Journal of Structural Geology, v. 18, no. 8, p. 1031–1042, doi:10.1016/0191-8141(96)00032-6.

Sipkin, S., 1985, Earthquake processes in the Long Valley Caldera area, California: Journal of Geophysical Research, v. 90, no. B13, p. 11155–11169, doi:10.1029/JB090iB13p11155.

Stein, S., and M. Wysession, 2003, An introduction to seismology, earthquakes, and earth structure: Malden, Massachusetts, Blackwell Publishing, 512 p.

Vavryčuk, V., 2001, Inversion for parameters of tensile earthquakes: Journal of Geophysical Research, v. 106, no. B8, p. 16,339–16,355, doi:10.1029/2001JB000372.

Vavryčuk, V., 2011, Tensile earthquakes: Theory, modeling, and inversion: Journal of Geophysical Research, v. 116, no. B12320, p 14.

Wallace, R. E., 1951, Geometry of shearing stress and relationship to faulting: Geology, v. 59, p. 111–130.

Warpinski, N. R., and L. W. Teufel, 1987, Influence of geologic discontinuities on hydraulic fracture propagation: Journal of Petroleum Technology, v. 39, no. 2, p. 209–220, doi:10.2118/13224-PA.

Williams-Stroud, S. C., and L. Eisner, 2010, Stimulated fractured reservoir DFN models calibrated with microseismic source mechanisms: American Rock Mechanics Association, 44th U.S. Rock Mechanics Symposium and 5th U.S.-Canada Rock Mechanics Symposium, Salt Lake City, Utah, June 27–30, 2010, 8 p.

Williams-Stroud, S. C., W. B. Barker, and K. L. Smith, 2012a, Induced hydraulic fractures or reactivated natural fractures? Modeling the response of natural fracture networks to stimulation treatments: American Rock Mechanics Association, 46th US Rock Mechanics/Geomechanics Symposium, Chicago, Illinois, June 24–27, 2012, 6 p.

Williams-Stroud, S. C., C. W. Neuhaus, C. Telker, C. Remington, W. Barker, G. Neshyba, and K. Blair, 2012b, Temporal evolution of stress states from hydraulic fracturing source mechanisms in the Marcellus shale: Society of Petroleum Engineers, SPE 162786, SPE Canadian Unconventional Resources Conference, Calgary, Canada, October 30–November 1, 2012, 6 p.

Zoback, M. D., A. Kohli, I. Das, and M. McClure, 2012, The importance of slow slip on faults during hydraulic fracturing stimulation of shale gas reservoirs: Society of Petroleum Engineers, SPE 155476, SPE Americas Unconventional Resources Conference, Pittsburgh, Pennsylvania, June 5–7, 2012, 9 p.